

Mechanisms of Confining Pressure Dependence of Resistivity Index for Tight Sandstones by Digital Core Analysis

Hongyi Dai, Igor Shikhov, and Rupeng Li, University of New South Wales; Ji-Youn Arns, CJEL Digital Imaging Education Solution Pty Ltd; and Christoph H. Arns, University of New South Wales

Summary

Resistivity measurements are a major input into hydrocarbon reserve estimation and are usually described by Archie's laws. In this study, we use digital rock physics to analyze the mechanisms of non-Archie and Archie behavior of formation factor (FF) and resistivity index (RI) of low-porosity Fontainebleau (FB) sandstone for ambient conditions and under high confining pressure, respectively.

FB sandstone was imaged by micro-X-ray computed tomography (micro-CT) at a resolution of 1 μm . Subresolution details of the grain contact width distribution along with their length were extracted from a set of scanning electron microscope (SEM) images. The nanoscale aperture of grain contacts, which is below tomogram resolution, is accounted for in micro-CT-based numerical calculations by assigning effective porosity and conductivity to individual voxels of the extracted grain contact network. A porosity reduction of grain contacts and open pore space as a function of applied confining pressure is introduced, capturing the pressure dependence. The concept was implemented by grain contact labeling, introducing an additional phase derived from a Euclidean distance transform (EDT). Sub-voxel stress-strain effects were incorporated by attributing all compressibility effects to the pore space (open pore space and grain contacts), treating the solid phase as perfectly rigid. Voxel-scale input conductivities are assigned using Archie's law followed by solving the Laplace equation for sample-scale rock resistivity and RI directly on the segmented image using the finite element method.

For the numerical modeling of the FF and RI of low-porosity FB sandstone as a function of confining pressure, which depends on subresolution features, a set of hypotheses were tested. These are based on two segmentation scenarios incorporating the measured contact aperture distribution from SEM analysis—a homogeneous aperture-based segmentation by assuming all grain contacts as an average constant value and a heterogeneous aperture-based segmentation assigning two groups of grain contact apertures. The segmentation scenarios enable homogeneous and heterogeneous morphological change of grain contacts due to confining pressure effects. Furthermore, partial saturation of grain contacts is considered. In all cases, strong water-wetness was assumed, and discretization effects were analyzed carefully.

The numerical results highlight the relative contribution of each of two conductive components of FB sandstone (open pores vs. grain contacts) over the full range of partial saturations. Of importance is the connectivity of the system, with discretization effects having a significant effect on FF, but a small effect on the RI. Grain contacts and confining pressure are found to have a significant impact on RI behavior of low-porosity FB sandstone. Both the grain contact network with homogeneous aperture and the heterogeneous grain contact network are able to describe experimental observations. However, it is not sufficient to assume a homogeneous change in contact area, and an inhomogeneous deformation of grain contact zones is required to match the experiment.

Introduction

Archie (1942) presented two significant empirical power law functions to describe the electrical resistivity behavior of reservoir rock. The first Archie equation governs the resistivity of fully brine-saturated reservoir rock, which is shown as

$$\text{FF} = \frac{R_o}{R_w} = \frac{a}{\phi^m} \quad \dots \dots \dots (1)$$

Here, FF is defined as the ratio of fully brine-saturated rock resistivity R_o to its same brine resistivity R_w , which also can be expressed as the reciprocal of the reservoir rock porosity ϕ to the power of the cementation exponent m . Variations of the preceding empirical correlation between FF and porosity ϕ for sandstones were proposed for various real reservoir data afterward (Winsauer et al. 1952; Porter and Carothers 1970; Timur et al. 1972). The second Archie equation expresses the change of resistivity due to changes in water saturation:

$$\text{RI} = \frac{R_t}{R_o} = S_w^{-n} \quad \dots \dots \dots (2)$$

Here, the RI is defined as the ratio of partially saturated (containing water and hydrocarbon) reservoir rock resistivity R_t to the fully brine-saturated rock resistivity R_o , also expressed as the reciprocal of the water saturation S_w to the power of the saturation exponent n . The value of n is normally assumed to be 2 for clean sandstone. Han et al. (2009), Montaron (2009), Kumar et al. (2011), and Yanici et al. (2013) demonstrated that deviations from Archie's behavior are known to occur, particularly at low water saturation, even for clean sandstones.

Yanici et al. (2013) investigated the RI behavior of strongly water-wet and clean higher-porosity FB sandstone ($\phi = 15\%$) at ambient pressure both experimentally and numerically, which confirmed the previous conclusion that FB sandstone shows non-Archie behavior at low water saturation (Durand 2003; Wilson 2004; Knackstedt et al. 2007; Han et al. 2009). Yanici et al. (2013) also concluded that the negative deviation of RI from Archie's law down to low water saturation at ambient conditions for FB sandstones is due to the presence of conductive percolating grain contact regions. Farid et al. (2016) examined this conclusion and further experimentally found that the effect of high confining pressure can weaken the non-Archie behavior of FB sandstone at low water saturation.

Numerically, micro-CT image-based RI simulations of FB sandstone at ambient condition matched laboratory data by introducing the concept of grain contact conductivity (Yanici et al. 2013). Farid et al. (2016) extended this work to low-porosity FB sandstone. However, grain contact aperture was not directly measured and porosity reduction with confining pressure not modeled. The modeling was not sufficiently constrained for clear conclusions about microscale mechanisms, and a match to experiment for RI calculations on low-porosity FB sandstone was not achieved.

In this paper, we propose a workflow for the FF and RI simulation of tight sandstone (FB) at both ambient and high confining pressure depending on the combined use of SEM analysis and micro-CT image-based calculation. Subresolution details of grain contact density and their aperture distribution of FB sandstone were extracted from a set of higher resolution 2D SEM images. A set of image-based calculations is performed to match the experimental data based on the extracted grain contact information and various segmentation strategies and grain partitioning scenarios. We first introduce the respective image processing steps, including the modeling of pressure-dependent voxel-scale porosity, followed by calculations of sample porosity, FF, and RI as a function of confining pressure.

Methodology

Rock Samples. FB sandstone is a very clean sandstone from the Ile-de-France region south of Paris. Xray diffraction (XRD) analysis indicated 99.3% quartz, 0.7% other minerals (mainly feldspar), and no clays. It is also well-sorted with an average grain size of approximately 250 μm (David et al. 1993). The porosity and permeability of FB sandstone ranges from 2 to 30% and 0.01 to 3000 md, respectively (Gomez et al. 2010; Al Saadi et al. 2017). In this work, we use the literature experimental data from one 1-in. diameter and two 1.5-in. diameter samples of extremely tight FB sandstone (4 to 5% porosity, 0.2- to 1.4-md permeability) (Farid et al. 2016).

Numerical Analysis Workflow. Fig. 1 displays the numerical analysis workflow of this study. For the strongly water-wet low-porosity FB sandstone considered here, we mainly focus on the effect of microstructure (grain contacts) and confining pressure on RI change. SEM characterization of grain contact aperture distribution is applied to constrain parameters of the micro-CT-based calculation. Micro-CT is then used to derive a high-resolution numerical 3D model incorporating the SEM-derived grain contact data. This is achieved through a series of image processing steps, including a morphological technique to mimic pore-scale confining pressure effects on porosity. Application of this model to the calculation of porosity, FF, and RI confirms findings of FB sandstone returning toward Archie behavior at higher confining pressures.

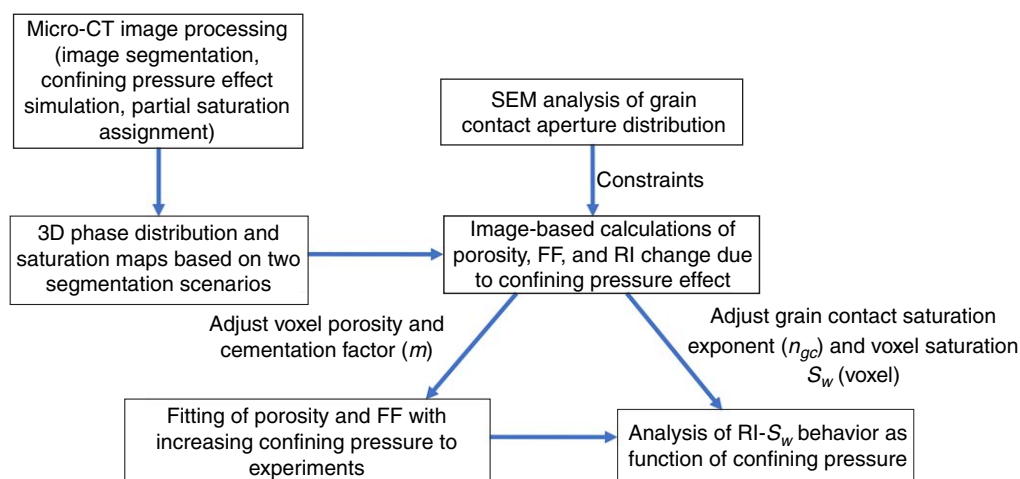


Fig. 1—Numerical analysis workflow of this work.

SEM Analysis of Grain Contact Aperture Distribution. First, a thin slice of the FB specimen was prepared and imaged with large field of view (Fig. 2a). Forty small parts of grain contacts were then selected at similar distance in a regular pattern (such as Fig. 2b). Based on the algorithm from Ronneberger et al. (2015), grain contacts of these 40 images were segmented out (Fig. 2c), and the image-noise and grain-pore space boundary were removed. After this binarization, the grain contact network of each image was extracted (Fig. 2d). For each extracted grain contact, we derived the medial axis points along with grain contact length. The medial axis points and each grain contact aperture are displayed in Fig. 2e. Finally, for the average grain contact aperture calculation, the grain contacts were labeled by number in each image (Fig. 2f). The grain contact apertures of each medial axis point in every grain contact were calculated by using vertical distance of each point between grain contact boundary multiplied by the corresponding slope of that point, and then multiplied by the image resolution (voxel length with the unit) according to

$$\text{Aperture} = \sin \frac{\pi}{2} \times d_v \times \text{slope} \times \text{resolution} \quad (3)$$

Here, aperture is the grain contact apertures through each medial axis point in every grain contact in μm ; d_v is the voxel-scale vertical distance (voxel number) of each point between the grain contact boundaries, which is perpendicular to horizontal axis, dimensionless; slope is the slope of each medial axis point along with the corresponding grain contact aperture, dimensionless; resolution is the real length of each voxel in image, $\mu\text{m}/\text{voxel}$; and $\sin(\pi/2)$ accounts for the average angle of the grain contact plane relative to direction of view. The statistics of grain contact aperture along each grain contact was acquired from SEM images with 40 small parts of grain contact. Fig. 3 shows the statistics of the 12 labeled grain contacts of Fig. 2 (voxel number of each grain contact aperture along with counting the median axis point in each grain contact). Fig. 4 depicts the final grain contact aperture distribution of these 40 small parts. Two groups of grain contact apertures were identified, with corresponding average grain contact apertures of $0.159 \pm 0.070 \mu\text{m}$ and $0.582 \pm 0.243 \mu\text{m}$ for the narrow and thick grain contacts, respectively. The total average grain contact aperture is $0.345 \pm 0.109 \mu\text{m}$. This grain contact distribution of FB sample is used to constrain the voxel-scale porosity and electrical conductivity of grain contacts in the following micro-CT-based calculations.

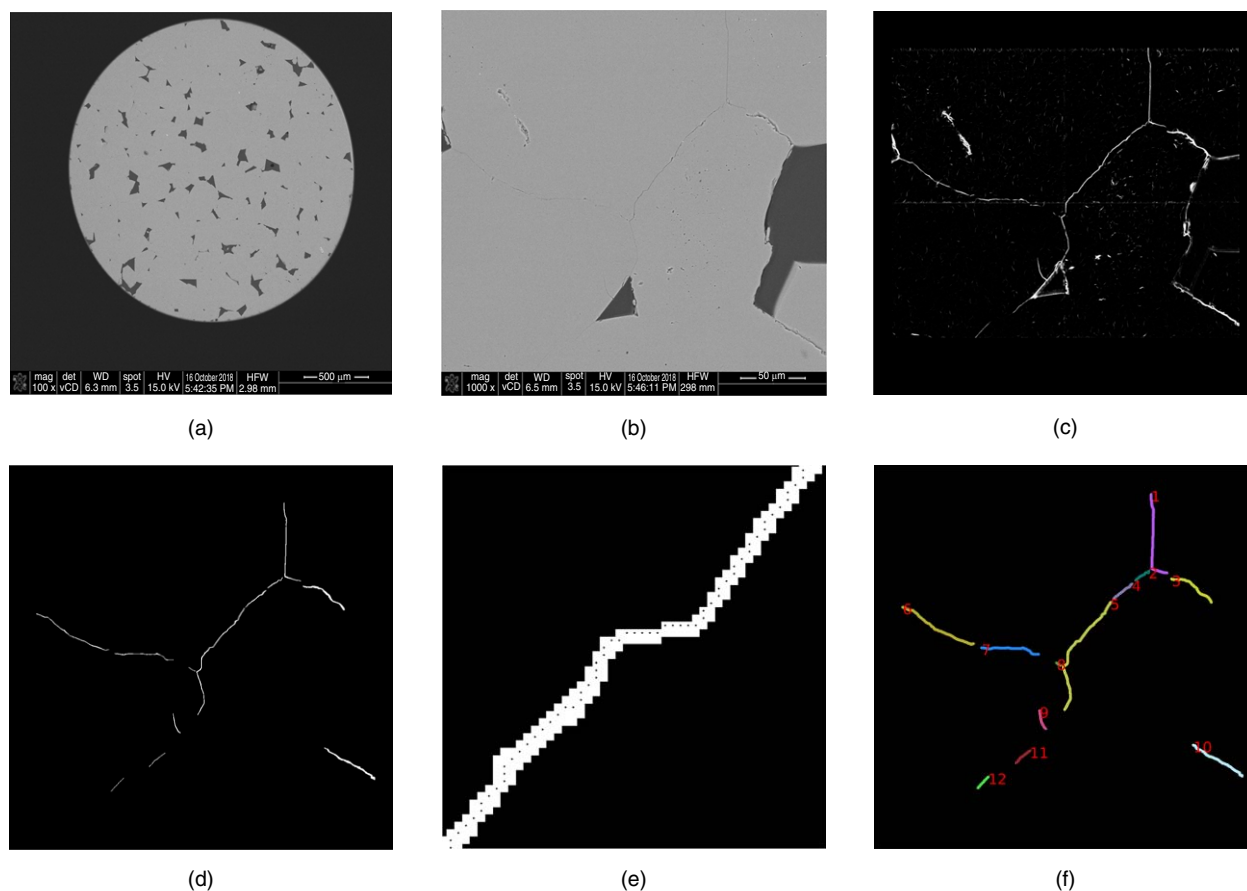


Fig. 2—SEM analysis of grain contact apertures: (a) large field of view SEM; (b) one of 40 small parts from this large field of view; (c) segmented grain contact network of this small part; (d) binarization and boundary, noisy part removal; (e) medial axis points defining local aperture (inscribed circle diameter); and (f) clustering of grain contact segments leading to average aperture distribution.

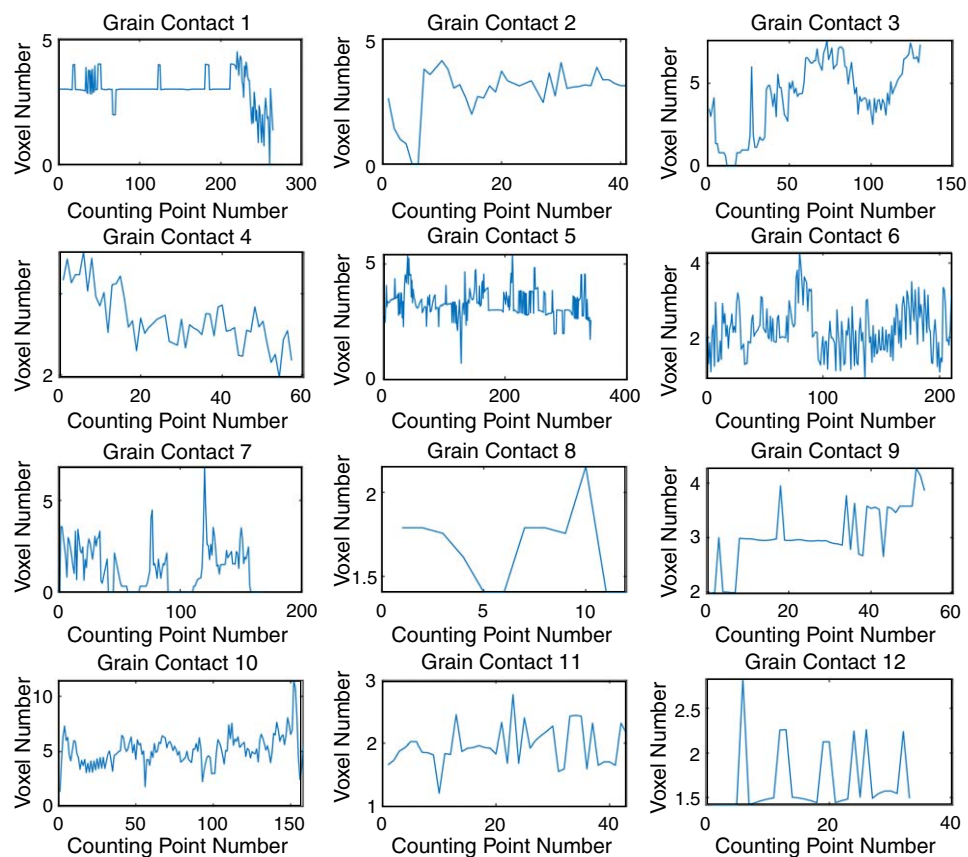


Fig. 3—Grain contact aperture along medial axis points for 12 labeled grain contacts (see Fig. 2f; units in voxel).

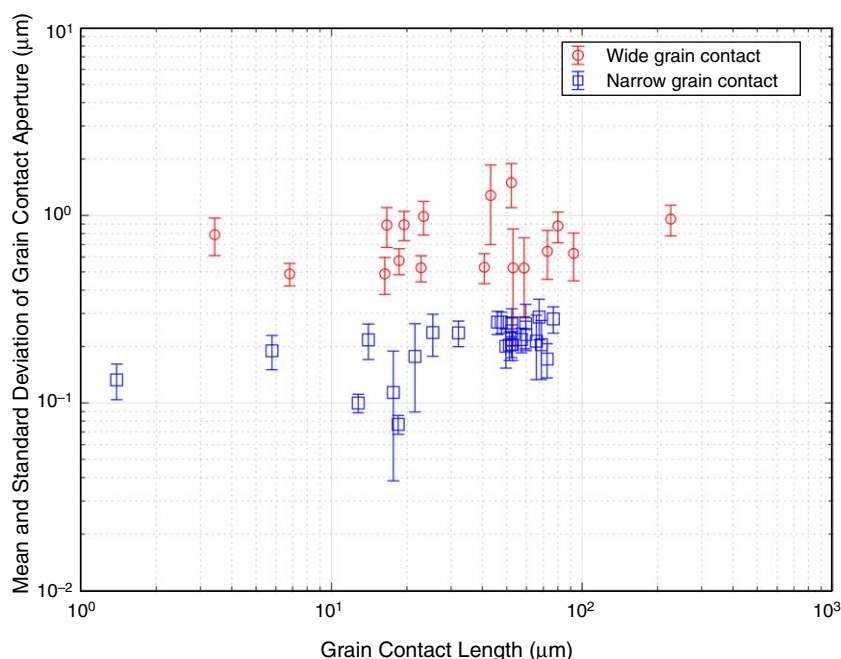


Fig. 4—Mean and standard deviation of grain contact aperture vs. the corresponding grain contact length for the 40 small parts of scanned FB sandstone sample.

Image-Acquisition and -Based Analysis. Image Acquisition. A 2-mm diameter 6-mm length FB sandstone sample was mounted on the top of the rotation stage at the XRD CT setup at the University of New South Wales (UNSW). It is equipped with a nano-focus X-ray tube (180 kV/15W with diamond windows) and a high-quality digital flat panel detector ($3,072 \times 3,072$ pixels, 3.75 fps readout rate). Radiographs of the sample were acquired at 80 kV X-ray energy using a 0.75-mm aluminum filter in double helix mode with a total acquisition time over 15 hours. Tomograms of dimension $1800 \times 2520 \times 2520$ voxel were reconstructed on the Australian National Computational Infrastructure using a modified Katsevich exact reconstruction algorithm for high-resolution helical cone-beam micro-CT (Katsevich 2004; Varslot et al. 2011).

Filtering and Segmentation. Optimum image quality depends not only on voxel size and spatial resolution but also image noise. Sprawls (1995) pointed out that image noise is defined as the random signal in image brightness, which could heavily weaken the image quality. It normally affects identification of the significant features in the initial image, if the noise is too high. Reddinger (1998) remarked that the cause of image noise mainly comes from CT facilities, such as energy undulation from the X-ray source, shortage of photon flux, and instability of beam intensity.

Digital (smoothing) filters were introduced to help mitigate image noise (Lee 1983). In this work, the three types of digital filters (modulated by local average, anisotropic diffusion, neighborhood filtering) in the Mango filter (Sheppard et al. 2004) that we implemented were primarily used for image denoising before image segmentation. Nixon and Aguado (2012) pointed out that the modulate-by-local-average filter regulates intensities across all the data sets through local averages with a Gaussian smoothing function applied in the image smoothing process, which weakens local noise and improves the quality of features. Depending on the selection of appropriate segmentation thresholds, an anisotropic diffusion filter assists in removing the remaining noise; it preserves the integral intensity and its key features and edges during the process of noise removal (Sheppard et al. 2004). Neighborhood filtering is used most of time, because other filters may generate blurring when denoising. This blur is mitigated by averaging the intensity of neighboring voxels (Buades et al. 2006). Image segmentation was carried out via the converging active contours algorithm developed by Sheppard et al. (2004). This approach enables growing intensity contours for the defined two thresholds (such as solid and grain) with the help of optional gradients (first-order neighboring differences) and optional additional thresholds to adjust the accuracy of segmentation.

Grain Partitioning and Phase Labeling. Grain partitioning starts at finding minima in the EDT of the grain phase from the center of grain. Danielsson (1980) introduced an exact EDT algorithm deriving the distance from each point in the phase of interest to the nearest phase boundary. The initial seeds in the grain phase are propagated by a converging active contour method operating on the grain phase (Sheppard et al. 2004; Saadatfar et al. 2005). After smoothing the EDT map, the watershed transformation is applied to convert the distance map into the labels file in which each watershed basin is given a separate label. A grain merging step is performed afterward to match grain contact density roughly with the SEM images by combining a labeling and region-merging algorithm implemented in Mango (Sheppard et al. 2006), which results in the labeled grain boundaries. A grain contact phase is then determined by selecting all voxels with different grain label neighbors. An overview of many of these techniques can be found in Sakellariou et al. (2007).

In this study, we consider two segmentation scenarios of FB sandstone incorporating both fine details visible in the tomogram (Fig. 5) due to its high resolution of $1 \mu\text{m}$ in contrast to previous studies, and the auxiliary SEM measurements constraining grain contact aperture.

Scenario 1 (S1): Based on image intensity and its gradient the tomogram (Fig. 5a shows one layer of z-slice initial tomogram) was initially segmented into three phases (normal grain, high-density grain, and pore space). We merged the high-density grain phase into the majority grain phase because it is irrelevant for electrical conductivity calculations (Fig. 5b). The grain contact network (Fig. 5d) was then generated by grain partitioning (Fig. 5c) and phase labeling. The advantage of this scenario is the relatively straightforward generation of the grain contact network by a morphological algorithm (Jones et al. 2009). The aperture of all grain contacts is assumed as a single constant value. In this scenario, some intermediate intensity voxels, which visibly form grain contacts, are merged into the solid phase because detection of the grain contact region is quite difficult.

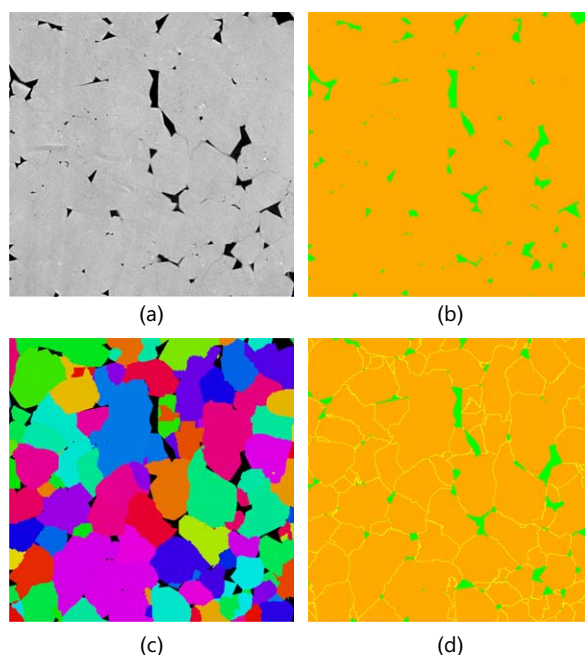


Fig. 5—The process of three-phase segmentation and single grain contact phase generation for segmentation S1 of FB sandstone (one z-direction slice through the volume of 1200^3 voxels): (a) initial tomogram of FB sandstone after image enhancement; (b) two-phase segmentation (green phase: bulk pore space, dark yellow: solid); (c) grain partitioning map by using the EDT and watershed transformation; and (d) the generation of grain contact network phase (light yellow).

Scenario 2 (S2): Given that two groups of grain contact apertures were recognized by SEM analysis, we extracted two types of grain contact phases (wide and narrow) by aggressively segmenting the pore space to force the direct detection of grain contacts. This scenario uses all the available intensity information in the image. Based on the two-phase segmentation (Fig. 5b), this resulted in a four-phase segmentation (Fig. 6c). The advantage of this scenario is a more truthful determination of the grain contact network because visible crevices are included and lead to better location of the morphologically determined grain contacts, which connect to the directly detected grain contact voxels. This scenario also makes use of the two grain contact aperture groups and thus enables consideration of grain contact aperture heterogeneity in the following image-based electrical property calculations (see Eq. 4). Fig. 6 illustrates the process of introducing these two different grain aperture groups.

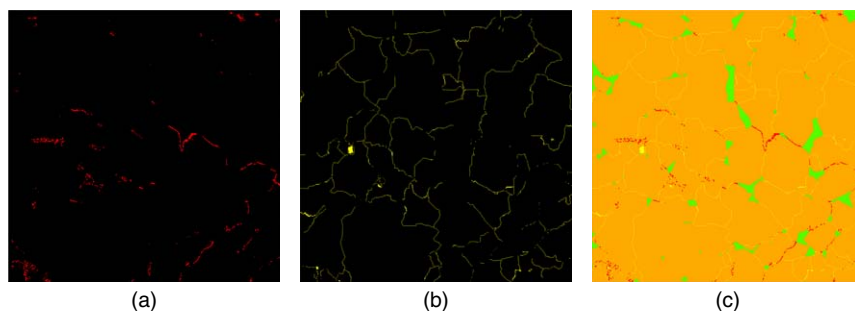


Fig. 6—The process of four-phase segmentation and dual grain contacts phases (narrow and wide) generation for segmentation S2 of FB sandstone (one z-direction slice through the volume of 1200^3 voxels): (a) wide grain contact phase generation; (b) narrow grain contact phase generation; and (c) the resultant four-phase segmentation (dark yellow: solid, green: open pore, red: wide grain contact, light yellow: narrow grain contact).

Electrical Properties Calculation. Electrical properties are calculated directly on the segmented images and phase distribution maps by using the voxel discretization naturally provided by the tomograms. Each voxel is assigned a distinct conductivity according to its phase label, and a finite element method used to solve the Laplace problem of electrical conductivity (Garboczi 1998; Arns et al. 2001). A potential drop is applied in the z-direction of the tomogram for the FB sandstone sample by assigning a constant potential of zero and unity to the inlet and outlet voxels, respectively. According to Eq. 1, FF based on the micro-CT image is obtained by the ratio of image-based water electrical conductivity σ_w to image-based fully saturated rock electrical conductivity σ_o . Here, σ_w is a constant value as unity, and σ_o is calculated by setting the conductivity of each voxel (voxel conductivity) of each phase in the calculation. For the input parameter set of FF calculations, the voxel conductivity σ_{voxel} of each conductive phase is consistent with its occupied voxel porosity ϕ_{voxel} powered by its cementation factor m (Eq. 4):

$$(\sigma_{\text{voxel}})_j = (\phi_{\text{voxel}})_j^m \cdot \dots \dots \dots (4)$$

Here, j stands for any conductive phase j , $(\phi_{\text{voxel}})_j$ is the voxel porosity of a conductive phase, and m is the cementation factor of a conductive phase. The voxel conductivity of the nonconductive phase (such as solid and nonwetting phase) is assumed as zero. Based on the saturation maps after image processing and Eq. 2, the RI of each saturation point is acquired by the ratio of fully saturated rock electrical conductivity ($S_w = 100\%$) and partially saturated rock conductivity ($S_w < 100\%$).

Simulation of Confining Pressure Effect. To develop an efficient simulation approach, the effect of confining pressure on the rock sample is approximated by using morphological change instead of solving a problem of a system mechanical deformation. It was experimentally demonstrated that the effect of increasing confining pressure on grain contacts results in the reduction of non-Archie behavior (Farid et al. 2016). This is likely due to a reduction of grain contact porosity by confining pressure, and thus the conductivity pathway of grain contact will be closed to some extent. However, the assumed closure of all grain contacts does not reproduce the reduction of porosity observed experimentally. Accordingly, a reduction in resolved open pore volume is also necessary. Therefore, two main components of the whole pore space within the FB sandstone sample—grain contacts (compliant) and open (bulk) pore—are compacted by elevated confining pressure.

The compaction of the open pore (macropore) phase is mimicked by a homogeneous contraction of the resolved open pore space by selecting the resolved pore voxels, which are directly adjacent to the solid. This is achieved by using an EDT and labeling them separately, which uses the new phase “pore-reduced volume phase” to numerically express the volumetric reduction of open pore by the elevated confining pressure. This enables a further reduction in pore space by assigning a porosity of each voxel (voxel porosity) that is smaller than unity to those resolved voxels, and in line with the pressure dependent reduction of grain contact aperture. Because grain contact aperture is small, the corresponding open pore space reduction is also small. Figs. 7 and 8 illustrate the concept of open pore space reduction with increasing confining pressure.

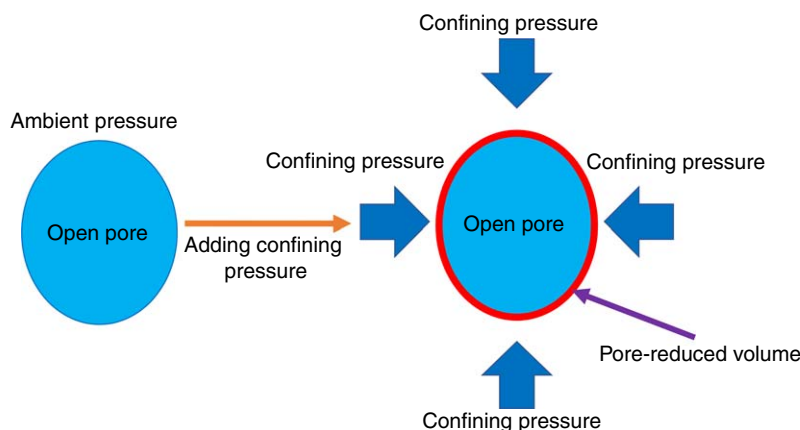


Fig. 7—Conceptual modeling of confining pressure effects for the image-resolved pore space.

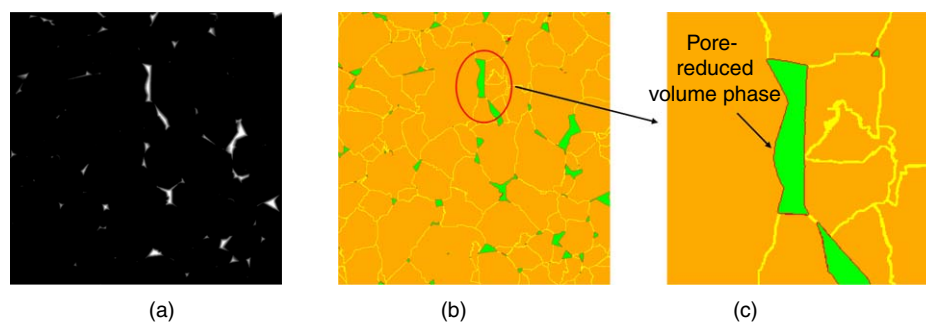


Fig. 8—Simulation of open pore space change by elevated confining pressure and the employment of the pore-reduced volume phase (one z-direction slice): (a) EDT map of FB sandstone; (b) four-phase distribution map (green: pore space, dark yellow: solid, light yellow: grain contact, red: pore-reduced volume); and (c) a small part from Fig. 8b shows the pore-reduced volume phase.

Fig. 9 presents the diagrams of two possible cases of confining pressure effect on grain contacts, which are uniform and heterogeneous morphological changes, respectively. In the uniform change case, confining pressure may only reduce the grain contact porosity and slightly affect the electrical conductivity provided by grain contact. However, confining pressure effect may result in the saturation change of the wetting fluid phase in the heterogeneous change case, because the middle part of the grain contact shown in Fig. 9c is closed much more than the outer part, and thus the invasion of nonwetting fluid is easier at partial saturations. Moreover, heterogeneous morphological change experienced by grain contacts may contribute worse electrical conductivity to the whole sample due to its possible blocked conductive pathway.

Partial Saturation Assignment for RI Calculation. Based on Hilpert and Miller (2001), Arns et al. (2005), and Shikhov and Arns (2013, 2015), the capillary drainage transform (CDT) can morphologically mimic the invasion of the nonwetting phase (oil or gas) in the imaged pore space of water-wet rock. We calculate the CDT on the bulk pore space of the full segmented images with mirror boundary conditions (we physically mirror the structure in all directions) and then use thresholds (radius of CDT, r_{CDT} , voxel-scale) to

set different saturations. The employment of mirror boundary is to eliminate the saturation boundary effect on the accuracy of the corresponding RI calculation at partial saturation. FB sandstone is an outcrop rock known to be strongly water-wet. To mimic partial saturations of the open pore space at elevated confining pressure, we also introduce the partial saturations into a pore-reduced volume phase by a CDT map. It results in four labels for the resolved pore space, two for each fluid (wetting and nonwetting, compacted and noncompacted). However, introducing partial saturations in grain contacts is not straightforward. It is expected that grain contacts can be effectively partially saturated due to the heterogeneous morphological change by confining pressure effect (Fig. 9c). It is necessary to test the possible saturation of grain contact phase at partial saturation because it will affect the change of electrical conductivity with increasing confining pressure. Nevertheless, partial saturation of grain contacts is difficult to directly simulate in the micro-CT image because the minimum voxel-scale radius of CDT cannot invade the grain contact phase. Saturation-dependent and pressure-dependent conductivity values for parts of grain contacts would have to be introduced, implying a range of free parameters. In the Results section, we present an alternative method to solve this problem (see RI Change with Increasing Confining Pressure). **Fig. 10** shows the CDT and various saturation maps and relabeled phases at different saturations (different radius of CDT) based on segmentation S1 of FB sandstone.

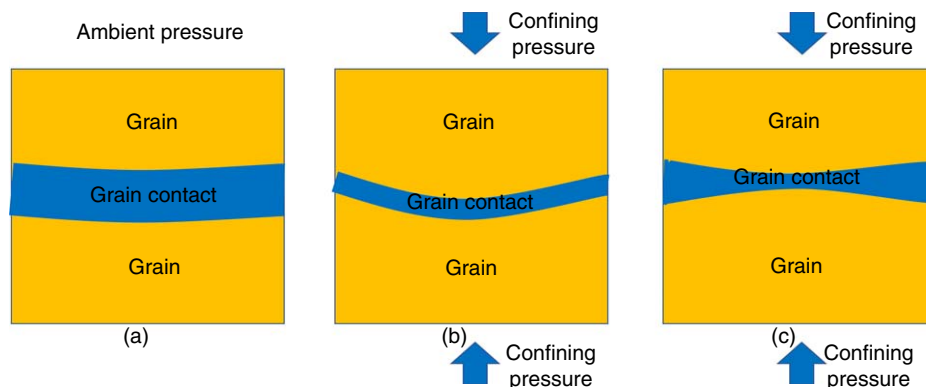


Fig. 9—Conceptual confining pressure effect on grain contacts: (a) grain contact at ambient condition, (b) uniform deformation of grain contact region, and (c) heterogeneous morphological change of grain contact.

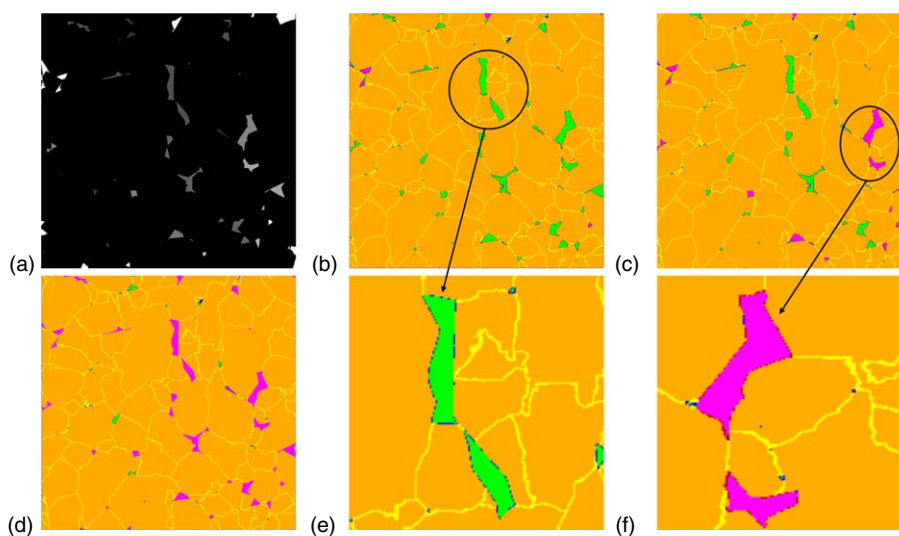


Fig. 10—(a) CDT map of FB sandstone (one z-direction slice, 1200^3 voxels); (b through d) phase distribution map at different water saturations ($S_w = 91, 52,$ and 22% , respectively); and (e through f) green: bulk pore phase of water, blue: pore-reduced volume of water, pink: bulk pore phase of nonwetting fluid, red: pore-reduced volume of nonwetting fluid, dark yellow: solid, light yellow: grain contacts.

The calculation of water saturations S_w at each different distance (radius of CDT) are performed by the ratio of the total porosity of wetting fluid phases ϕ_{water} to total connected porosity ϕ_t through the whole image of the sample:

$$S_w = \frac{\phi_{\text{water}}}{\phi_t} \quad \dots \dots \dots (5)$$

Here, S_w is the total water saturation calculated from the set of one radius of CDT, ϕ_{water} is the sum of total porosity of wetting fluid phase, and ϕ_t is the total porosity of the sample from micro-CT image.

Discretization Effects. Discretization effects are inevitable due to limited image resolution for thin conductors, which will affect the accuracy of simulation to some extent. To evaluate this effect within a practical range of resolutions and resulting computational

effort, the initial tomogram of FB sandstone was resampled by a factor of 2 by interpolating the gray-scale tomogram directly. This reduced the voxel size from 1 to 0.5 μm and enlarged the image dimensions from $1,800 \times 2,520 \times 2,520$ voxels to $3,600 \times 5,040 \times 5,040$ voxels, respectively. All the following image processing steps (image enhancement and segmentation, grain partitioning, mirroring, the generation of EDT, CDT, phase distribution maps, etc.) were performed on both image dimensions. To observe the degree of discretization effect, we present four cases of numerical results (both 1200^3 and 2400^3 voxels for each segmentation scenario) for FB sandstone in this work. It is important to note that the 1200^3 and 2400^3 sections represent an inner cube after CDT-based saturation calculations, avoiding invasion boundary effects.

S1 and S2 imply slightly different discretization problems because S1 morphologically derived grain contacts are two voxels thick by construction, while for S2, the thick grain contacts are “too thick” due to the aggressive segmentation strategy, and conductivities need to be reduced accordingly, while the thin contacts are only 1 voxel thick.

Results

Porosity Change with Elevated Confining Pressure. In the image-based porosity calculation of the FB sample, voxel porosity of solid (grain) was set as zero, and the voxel porosity of open pore space and pore-reduced volume phase were unity at ambient pressure. However, voxel porosity of grain contact phase was introduced, because average grain contact aperture obtained from SEM analysis is smaller than one voxel size (1 μm). For various segmentation scenarios and simulation cases, the set of grain contact voxel porosities and their change were dominated by grain contact aperture distribution, the magnitude of confining pressure, and voxel size.

The mean values of grain contact aperture based on SEM analysis were applied and converted into voxel porosities in the porosity calculations of both segmentation scenario S1 and S2 at ambient pressure. For example, the mean value of grain contact aperture is 0.436 μm in the segmentation scenario S1, and the converted grain contact voxel porosity is 0.218 given that the grain contact occupies two voxels because the image voxel size is 1 μm .

To accurately represent confining pressure effects on porosity and match to experimental data, the voxel porosity of the grain contact phase was adjusted within the constraint range of grain contact aperture distribution (0.345 ± 0.109 μm for average single grain contact aperture ranges, 0.159 ± 0.070 μm and 0.582 ± 0.243 μm for the average narrow and thick grain contact aperture ranges, respectively) from SEM analysis at ambient pressure and the continuous decrease of grain contact voxel porosity at each elevated confining pressure point (from 0 to 6000 psi) tested for each case. Importantly, the voxel porosity reduction of the pore-reduced volume phase is different for S1 and S2. In S1, voxel porosity reduction of the pore-reduced phase is consistent with the grain contact voxel porosity because it assumed that pore space and grain contact are uniformly compressed by confining pressure. For S2, voxel porosity reduction of the pore-reduced phase is the average voxel porosity reduction of the narrow- and wide-grain contact phases. For instance, voxel porosity of grain contact and the pore-reduced volume phase are 0.218 and unity at ambient pressure in S1. Then in setting 0.187 as the voxel porosity of grain contact phase at 500 psi confining pressure, the corresponding voxel porosity of the pore-reduced phase is equal to 0.969, which it is calculated by $1 - (0.218 - 0.187)$. The phase labeling and voxel porosity set of each phase for both segmentation scenarios from ambient to elevated confining pressures are tabulated in **Tables 1 and 2**. **Fig. 11** shows the determinations of grain contact and the pore-reduced volume voxel porosity at different confining pressures by matching the numerical results of porosity change to experimental data. An excellent match is achieved within the constraints of the SEM-derived grain contact aperture. The confining pressure dependence can be modeled well by reducing this aperture as a function of confining pressure with associated reduction of porosity in the open pore space.

Phase	Label	Voxel Porosity	Voxel Conductivity (full saturation)	Voxel Conductivity (partial saturation)
Open pore	1	1	1	1
Solid (grains)	2	0	0	0
Grain contacts	3	The converted values based on average grain contact aperture from SEM analysis	$\sigma_{v,gc} = (\phi_{v,gc})^{m_{gc}}$	$\sigma_{v,gc} = \phi_{v,gc}^{m_{gc}} * (S_w - \text{voxel})^{n_{gc}}$
Pore-reduced volume	4	$^{**}(\phi_{v,pr})_{p_{conf}} = 1 - \Delta\phi_{v,gc}$	$\sigma_{v,pr} = (\phi_{v,pr})^m (m=1)$	$\sigma_{v,pr} = \phi_{v,pr}^m (m=1)$
Nonwetting fluid	5	1	0	0
Pore-reduced volume of nonwetting fluid	6	$(\phi_{v,pr})_{p_{conf}} = 1 - \Delta\phi_{v,gc}$	0	0

*v = voxel-scale, pr = pore-reduced volume phase, gc = grain contact phase

** $(\phi_{v,pr})_{p_{conf}}$ stands for the voxel porosity of pore-reduced volume or nonwetting fluid pore-reduced volume phase at one specific confining pressure from 0 to 6,000 psi; $\Delta\phi_{v,gc}$ stands for the voxel porosity reduction of grain contact phase between one pressure to the other increased confining pressure.

Table 1—Phase labeling, voxel porosity ϕ_{voxel} , and voxel conductivity σ_{voxel} set of FB sandstones based on segmentation S1.

FF Change with Increasing Confining Pressures. In the FF calculation, the cementation factors m of open pore space and the pore-reduced phase are assumed as unity, with the voxel conductivity of these two phases consistent with their voxel porosity. For example, voxel porosity of the bulk pore space phase and pore-reduced volume are equal to unity and 0.969 at 500 psi confining pressure, resulting in the voxel conductivity of unity and 0.969, respectively, because they are fully saturated with brine following Eq. 1. The respective m for the grain contact phase is set to match with the experimental data of the FF with increasing confining pressure from 0 to 6,000 psi. The voxel conductivity reduction of the grain contact phase is also consistent with the corresponding reduced voxel porosity powered by the grain contact cementation factors m_{gc} with increasing confining pressure. Voxel conductivities at full saturation

($S_w = 100\%$) for both segmentation scenarios are given in Tables 1 and 2. Based on the resultant 3D phase distribution maps at full saturation, different m_{gc} are tested for S1. Fig. 12 depicts the resultant FF change with increasing confining pressures and comparisons to experimental data.

Phase	Label	Voxel Porosity	Voxel Conductivity (full saturation)	Voxel Conductivity (partial saturation)
Open pore	1	1	1	1
Solid (grains)	2	0	0	0
Wide grain contacts	3	The converted values based on average grain contact aperture from SEM analysis	$\sigma_{v,wgc} = (\phi_{v,wgc})^{m_{gc}}$	$\sigma_{v,wgc} = \phi_{v,wgc}^{m_{gc}} * (S_{w-voxel})^{n_{gc}}$
Narrow grain contacts	4	The converted values based on average grain contact aperture from SEM analysis	$\sigma_{v,ngc} = (\phi_{v,ngc})^{m_{gc}}$	$\sigma_{v,ngc} = \phi_{v,ngc}^{m_{gc}} (S_{w-voxel})^{n_{gc}}$
Pore-reduced volume	5	$* * (\phi_{v,pr})_{p_{conf}} = 1 - \frac{\Delta\phi_{v,wgc} + \Delta\phi_{v,ngc}}{2}$	$\sigma_{v,pr} = (\phi_{v,pr})^m (m=1)$	$\sigma_{v,pr} = \phi_{v,pr}^m (m=1)$
Nonwetting fluid	6	1	0	0
Pore-reduced volume of nonwetting fluid	7	$(\phi_{v,pr})_{p_{conf}} = 1 - \frac{\Delta\phi_{v,wgc} + \Delta\phi_{v,ngc}}{2}$	0	0

*v = voxel-scale, pr = pore-reduced volume phase, gc = grain contact phase

** $(\phi_{v,pr})_{p_{conf}}$ stands for the voxel porosity of pore-reduced volume or nonwetting fluid pore-reduced volume phase at one specific confining pressure from 0 to 6,000 psi; $\Delta\phi_{v,gc}$ stands for the voxel porosity reduction of grain contact phase between one pressure to the other increased confining pressure.

Table 2—Phase labeling, voxel porosity ϕ_{voxel} , and voxel conductivity σ_{voxel} set of FB sandstones based on segmentation S2.

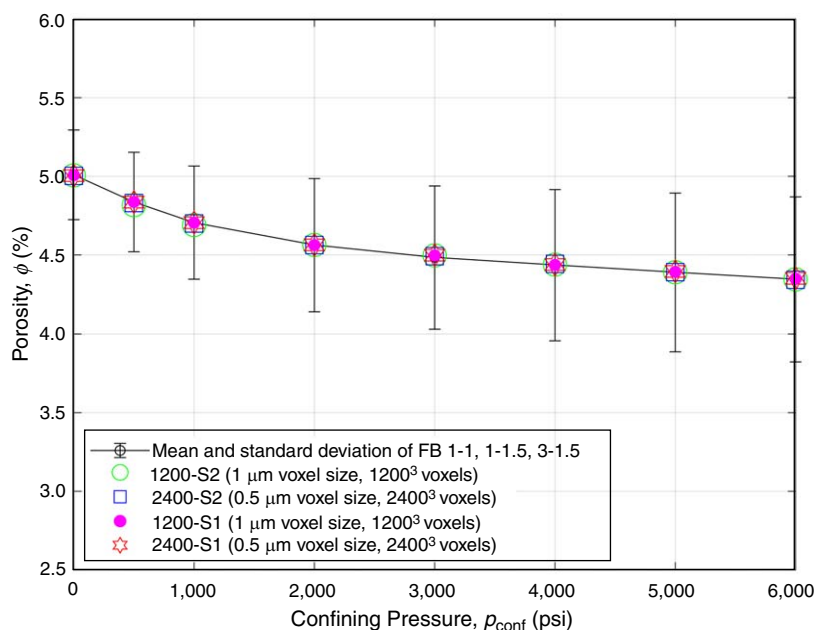


Fig. 11—Determinations of grain contact and pore-reduced volume voxel porosity with increasing confining pressures from 0 to 6,000psi by fitting numerical results of porosity change with experimental data for different cases (1200-S1 and 2400-S1 cases stand for 1 and 0.5μm voxel size of segmentation S1; 1200-S2 and 2400-S2 cases stand for 1 and 0.5μm voxel size of segmentation S2).

In Fig. 12a, it can be observed that numerical results of both 1200³ (1 μm voxel size) and 2400³ (0.5 μm voxel size) voxels at higher confining pressure (from 3,000 to 6,000 psi) in segmentation S2 can roughly fit with the experiment data for $m_{gc} = 1$. However, there is still a clear deviation between numerical results and experimental data from 0 to 2,000psi in S2. FF values for S1 (both 1200³ and 2400³ voxels) from 0 to 6,000psi confining pressures are too low compared with experimental data. The single grain contact of S1 displays better grain contact connectivity and uniformity, which results in the corresponding higher electrical conductivity compared with the dual grain contact network (S2). Given this, a higher cementation factor m_{gc} of the grain contact phase, independent of confining pressure, is determined to match the experimental data of FF change for the S1 case. Fig. 12b shows this match of FF change with increasing confining pressure for S1 cases ($m_{gc} = 1.34$ for 1 μm voxel size, 1200³ voxels and $m_{gc} = 1.44$ for 0.5 μm voxel size, 2400³ voxels, respectively).

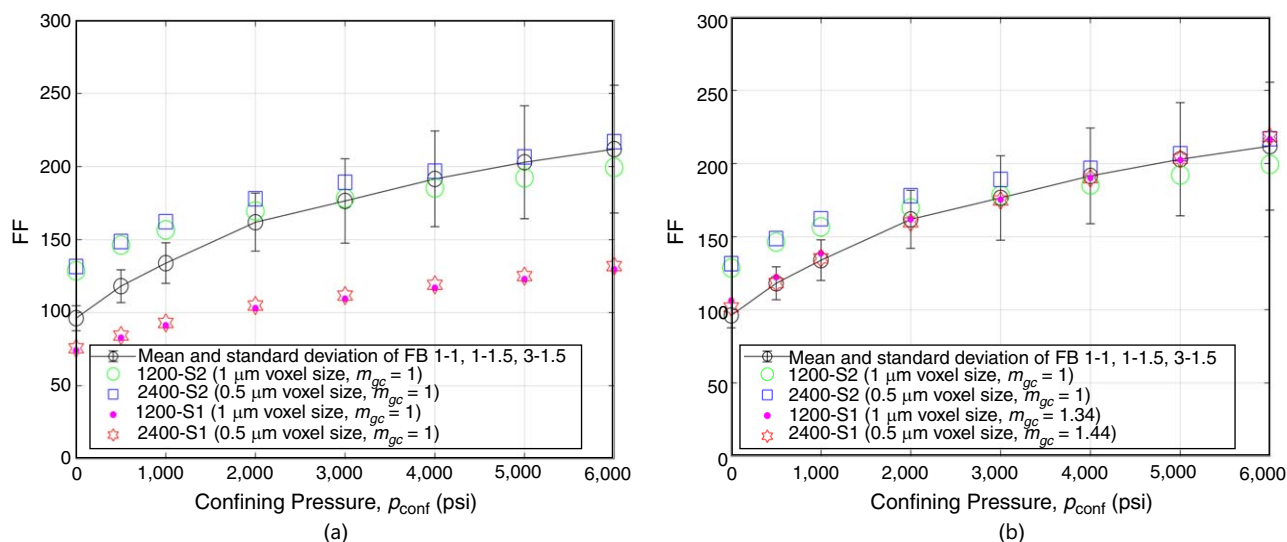


Fig. 12—Comparison of FF change with increasing confining pressures from 0 to 6,000 psia between numerical results and experimental data: (a) m_{gc} = unity and (b) by using m_{gc} as free parameter. 1200-S1 and 2400-S1 stand for 1 and 0.5 μm voxel size of segmentation S1; 1200-S2 and 2400-S2 stand for 1 and 0.5 μm voxel size of segmentation S2.

RI Change with Increasing Confining Pressures. Based on the uncertainty of grain contact saturation previously mentioned, grain contact may be full of wetting fluid even at low water saturation, or it can also be invaded by nonwetting fluid at high water saturation due to confining pressure effect. In this work, we propose two hypotheses to test the possible saturation of grain contact at partial saturation by image-based RI calculations.

Hypothesis 1. The grain contact phase is assumed to be fully saturated with the wetting fluid at all saturations. Partial saturations are solely a function of the saturation of the resolved pore space. In this hypothesis, the voxel conductivity of each conductive phase still follows Eq. 4 at different partial saturations. RI numerical results based on this hypothesis for both segmentation scenarios display strong deviations from experimental data at both 500 and 6,000 psi confining pressures (**Fig. 13**).

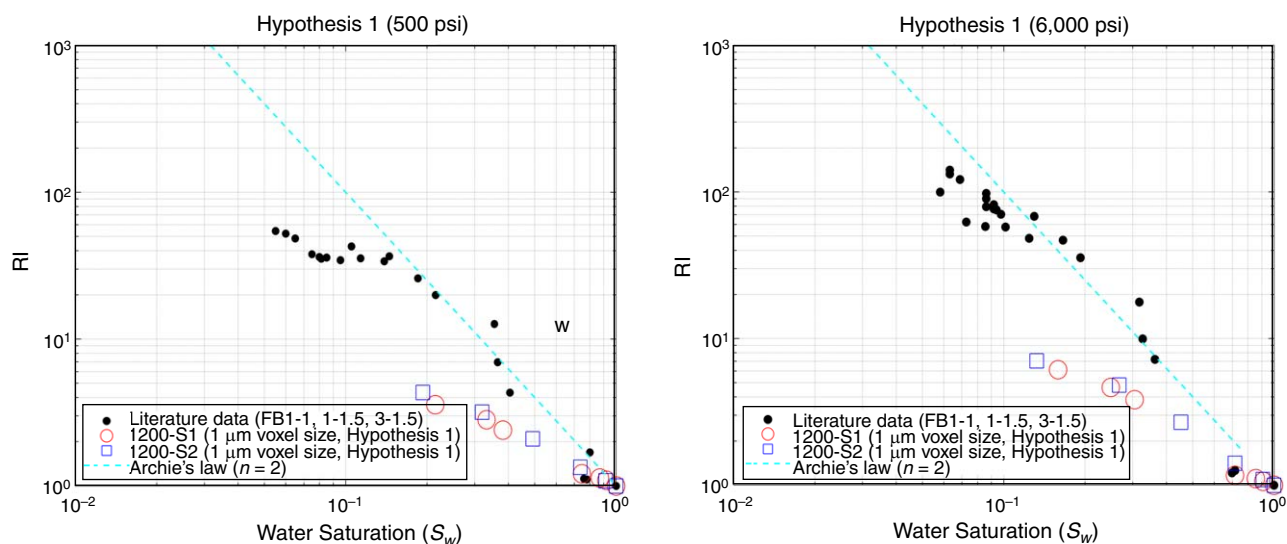


Fig. 13—Nonmatching RI- S_w curves between literature data and numerical results based on Hypothesis 1 of both segmentation scenarios (1200-S1: 1 μm voxel size, S1; 1200-S2: 1 μm voxel size, S2) at (a) 500 psi and (b) 6,000 psi confining pressures, respectively.

Hypothesis 2. Here the presence of saturation change for the grain contact phase at different partial saturations of the whole sample is assumed. This approach would require one of two possible explanations for the effective grain conductivity being saturation dependent at low capillary pressures. The first possibility is that the grain contact regions are considered mixed-wet, which we assume not to be true but cannot disprove either. The alternate explanation is that the outer rim of contact regions (Fig. 9c) has a larger angle for entry of the nonwetting phase. With the confining pressure increasing, this opening angle may widen, while at the same time the actual grain contact area grows and the grain contact aperture reduces (Hertz-Mindlin contact). It is a bit like pushing a fingertip and thumb together. This changes the balance such that quite high nonwetting fluid saturations are possible. Because the grain contact is an effective conductivity element as a whole, the actual water connectivity within the element also plays a role.

To investigate the possible partial saturation of grain contact phase and its effect on RI change, in this work we used two important parameters: one is voxel saturation $S_{w\text{-voxel}}$, and the other is the grain contact conductive exponent n_{gc} . Voxel saturation is defined as the wetting fluid saturation in grain contacts at partial saturation of the whole sample. Given the possible difference of electrical conductivity contribution to the whole sample between pore space and the grain contact phase, the grain contact conductive exponent is a variable that is used to express the conductive capability of the grain contact phase. Its magnitude is related to the connectivity and surface roughness of the grain contact network. The larger n_{gc} means worse connectivity or a rougher surface of the grain contact phase and therefore leads to the corresponding lower electrical conductivity.

Based on the preceding assumptions of RI calculation for Hypothesis 2, the voxel conductivity for pore space and pore reduction of the wetting fluid phase are consistent with Eq. 4. The other nonconductive phase (such as solid, nonwetting fluid, and the pore reduction of the nonwetting fluid) is always set as zero. Nevertheless, the voxel saturation $S_{w\text{-voxel}}$ as mentioned should be involved in the voxel conductivity of the grain contact phase at partial saturations, which is shown in Eq. 6:

$$\sigma_{\text{voxel}} = (\phi_{\text{voxel}})^{n_{gc}} \times (S_{w\text{-voxel}})^{n_{gc}} \quad \dots \dots \dots (6)$$

Hypothesis 2 numerical results and experimental data of RI based on segmentation S1 and S2 were compared at two different voxel sizes (1 and 0.5 μm) by testing the n_{gc} and $S_{w\text{-voxel}}$ of the corresponding conductive phases. This voxel conductivity set at partial saturation ($S_w < 100\%$) for both segmentation scenarios are detailed in Tables 1 and 2.

To investigate the grain contact conductive capability and the possible confining pressure effect on electrical conductivity of this phase based on Hypothesis 2, this work first tested various grain contact conductive exponents n_{gc} by roughly fitting with the RI literature data. Suitable voxel saturations $S_{w\text{-voxel}}$ of the corresponding phases at each saturation point were determined by matching the experimental data of RI- S_w curves at both 500 and 6,000 psi confining pressures based on two segmentation scenarios. **Fig. 14** shows the effect of the grain contact conductive exponent n_{gc} on RI at 500 psi confining pressure based on segmentation scenario S1. It provides strong evidence that the grain contact saturation is a controlling factor in the overall RI response of tight sandstone; for $n_{gc} = 2$, a good match with the experiment is achieved.

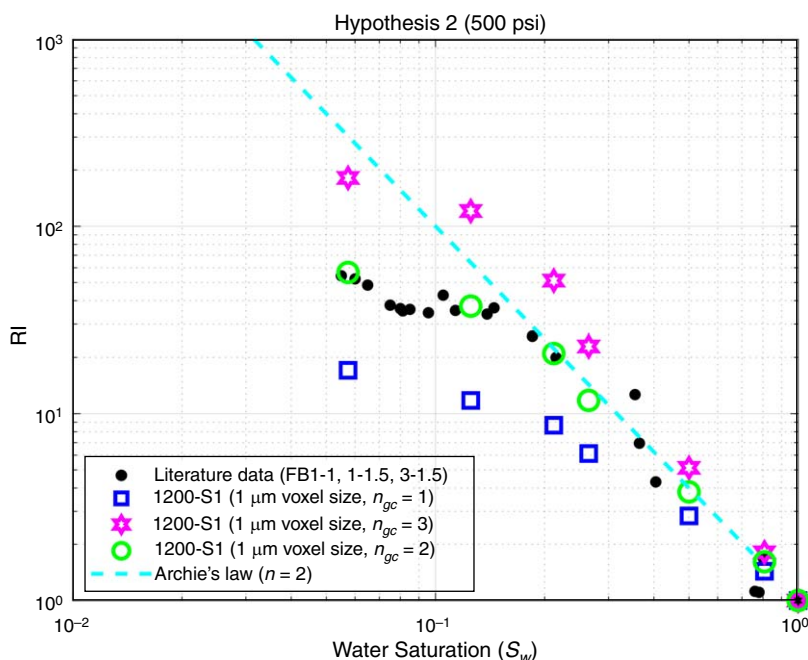


Fig. 14—Effect of grain contact conductive exponent n_{gc} on RI change based on segmentation S1 (1200-S1 stand for 1 μm voxel size, 1200³ voxels of segmentation S1).

Fig. 15 displays the relationships between grain contact water saturation $S_{w,gc}$ and capillary radius R at 500 and 6,000 psi confining pressures based on the tested optimum grain contact saturation determination of each saturation point (fitting RI numerical results to literature data) in both segmentation S1 and S2. It can be observed that the wide grain contact saturation shows a smaller variation range at 6,000 psi confining pressure compared with 500 psi, while the narrow grain contacts show the opposite behavior. Given the proposed cases that confining pressure effect can cause both homogeneous and heterogeneous morphological change of grain contact regions, one possible explanation is that the presence of uniform porosity reduction may occur tendentially more in wide grain contacts and heterogeneous morphological change preferentially in narrow grain contacts. This leads to the comparably easier invasion of narrow grain contacts by nonwetting fluid with increasing confining pressure. Using such a grain contact partial saturation approach (**Fig. 16**) displays an excellent match of RI- S_w curves between numerical results and literature experimental data at 500 and 6,000 psi confining pressure for FB sandstone, respectively.

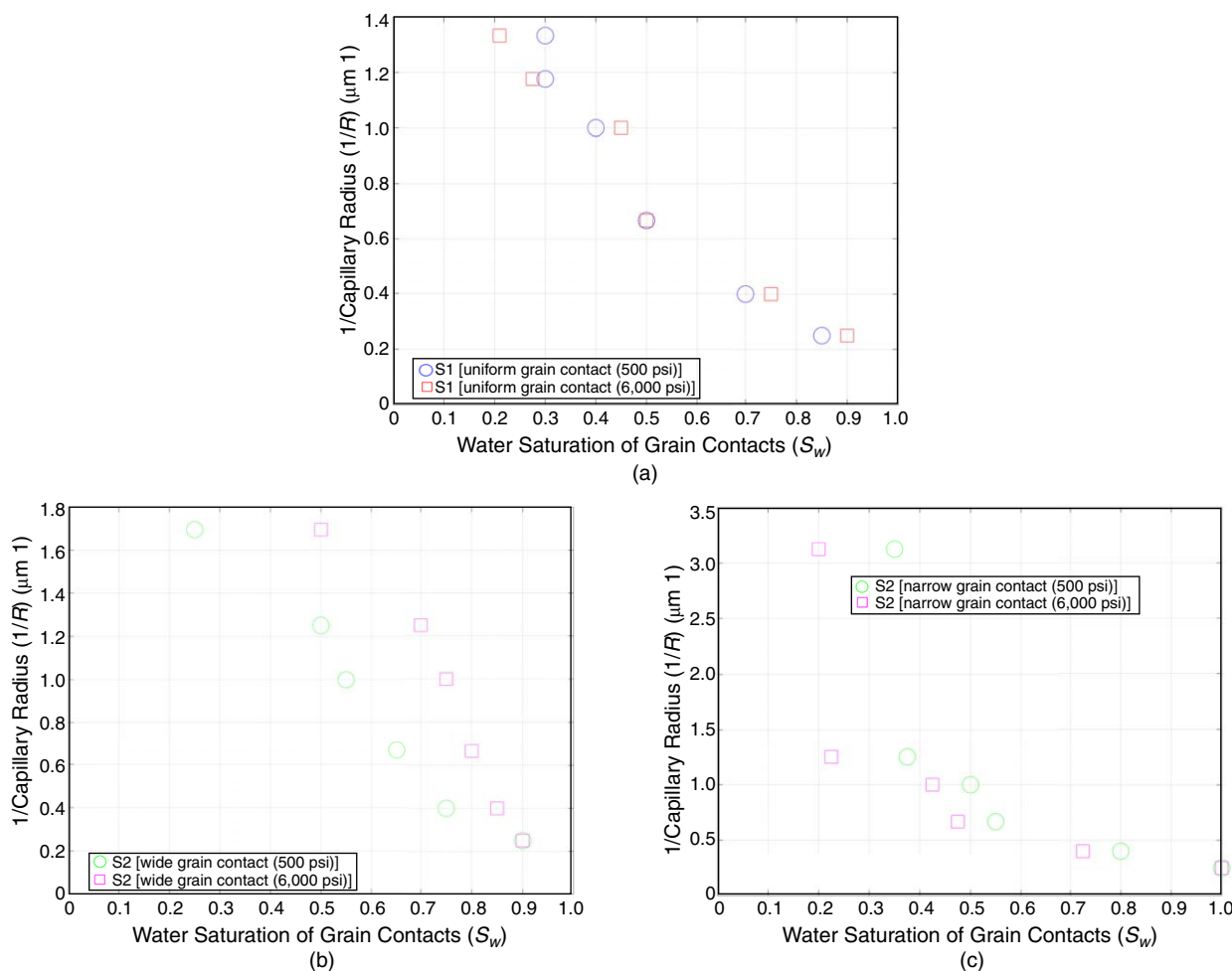


Fig. 15—Relationship between grain contact water saturation $S_{w,gc}$ and capillary radius R of both S1 and S2 based on the optimum grain contact determination of each saturation point: (a) uniform single grain contact in S1; and (b) (c) wide and narrow grain contacts in S2, respectively.

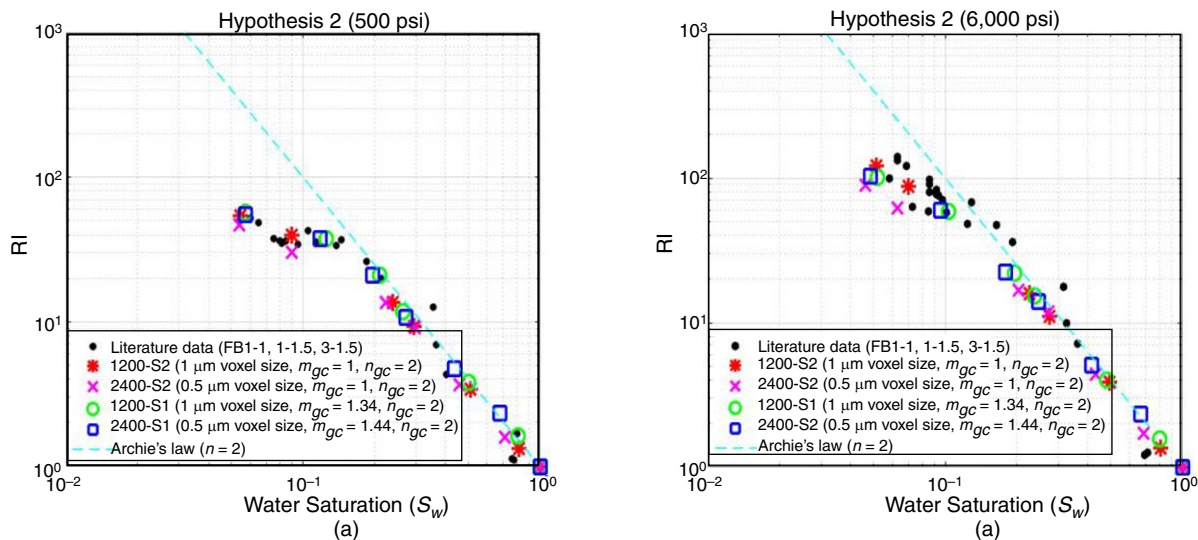


Fig. 16—Matching of RI - S_w curves between numerical results and experimental data for FB sandstone at (a) 500 and (b) 6,000 psi confining pressure (1200-S1 and 2400-S1 cases stand for 1 and 0.5 μm voxel size of segmentation S1; 1200-S2 and 2400-S2 cases stand for 1 and 0.5 μm voxel size of segmentation S2), respectively.

Conclusions

In this work, we analyzed the pressure dependence of electrical properties of FB sandstone based on SEM-derived grain contact aperture distributions and micro-CT-based numerical simulations. For low-porosity sandstone, the mechanisms for non-Archie RI behavior are challenging to model because microstructural features below the resolution of the tomogram (which was taken at the resolution limit of current generation micro-CT imaging devices) are relevant for RI calculations. It is further clear that actual measurements can only be matched by assuming both a heterogeneous deformation of grain contacts and at least homogeneous contraction of the resolved pore space. We comment on assumptions made in this work and future work:

1. Confining pressure effects on open pore space and grain contacts were numerically captured by using morphological change of volume (porosity reduction) instead of mechanical compaction by contact mechanics. To perfectly match with experimental RI behavior, a heterogeneous deformation of narrow grain contacts and homogeneous contraction of wide grain contacts or resolved open pore space was required because only then an effective partial saturation within grain contacts could be introduced; *effective* partial saturation in a grain contact requires either mixed wettability within grain contacts or a change of the entry aperture angle into the grain contact regions, which would be a function of confining pressure. The predictive modeling of RI for tight sandstones (with grain contacts) remains a very challenging task: from this study, it is clear that while numerical parameters can be found to match experiment, a still more sophisticated characterization and associated simulation approach would be required to calculate RI correctly for low-porosity FB sandstones.
2. The current analysis considers experiments under hydrostatic conditions. For a full treatment and match to experiment from first principles, a numerical model including contact mechanics may be necessary. This, however, does pose a serious characterization problem, which was out of scope for this work, given the already quite serious computational efforts, which were required to carry out the presented sensitivity studies on a representative volume element for comparison to experiment.
3. One may consider directly estimating the porosity reduction of pore space and grain contacts from a high-pressure registered image of FB sandstone. It is noted, however, that part of the experimental section of this work (not presented) was to attempt to directly detect grain contacts by differential imaging at ambient conditions, which was not successful. A direct imaging approach would require a further increase of resolution while keeping the same physical field of view. Such systems may eventuate with further detector development and extreme mechanical stability of X-ray CT systems, as may be expected from nano-CT technology at the cost of long imaging times.

Acknowledgments

Author CHA acknowledges the Australian Research Council (DP160104995) for funding. We would like to thank the Tyree X-ray Laboratory at the School of Minerals and Energy Resources Engineering, UNSW, for their assistance in micro-CT imaging. We also wish to thank MPhil Mikhail Farid from the Faculty of Engineering, UNSW, for experimental data support, and Dr. Yin Yao from the Electron Microscope Unit, Mark Wainwright Analytical Centre, UNSW, for assisting with FESEM. This research was undertaken with the assistance of resources from the National Computational Infrastructure (NCI Australia), an National Collaborative Research Infrastructure Strategy-enabled capability supported by the Australian Government, through Merit Grant m65.

References

- Al Saadi, F., Wolf, K., and Kruijsdijk, C. V. 2017. Characterization of Fontainebleau Sandstone: Quartz Overgrowth and Its Impact on Pore-Throat Framework. *J Pet Env Biotech* **8** (3): 1–12. <https://doi.org/10.4172/2157-7463.1000328>.
- Archie, G. E. 1942. The Electrical Resistivity Log as an Aid in Determining Some Reservoir Characteristics. In *Transactions of the Society of Petroleum Engineers*, Vol. 146, Part 1, SPE-942054-G, 54–62. Richardson, Texas, USA: Society of Petroleum Engineers. <https://doi.org/10.2118/942054-G>.
- Arns, C. H., Knackstedt, M. A., and Martys, N. S. 2005. Cross-Property Correlations and Permeability Estimation in Sandstone. *Phys Rev E* **72** (4): 46304. <https://doi.org/10.1103/PhysRevE.72.046304>.
- Arns, C. H., Knackstedt, M. A., Pinczewski, M. V. et al. 2001. Accurate Estimation of Transport Properties from Microtomographic Images. *Geophys Res Lett* **28** (17): 3361–3364. <https://doi.org/10.1029/2001GL012987>.
- Buades, A., Coll, B., and Morel, J. M. 2006. Neighborhood Filters and PDE's. *Numerische Mathematik* **105** (1): 1–34. <https://doi.org/10.1007/s00211-006-0029-y>.
- Danielsson, P. E. 1980. Euclidean Distance Mapping. *Comput Graphics Image Process* **14** (3): 227–248. [https://doi.org/10.1016/0146-664X\(80\)90054-4](https://doi.org/10.1016/0146-664X(80)90054-4).
- David, C., Darot, M., and Jeannette, D. 1993. Pore Structures and Transport Properties of Sandstone. *Transp Porous Media* **11** (2): 161–177. <https://doi.org/10.1007/BF01059632>.
- Durand, C. 2003. Combined Use of X-Ray CT Scan and Local Resistivity Measurements: A New Approach to Fluid Distribution Description in Cores. Paper presented at SPE Annual Technical Conference and Exhibition, Denver, Colorado, USA, 5–8 October. SPE-84299-MS. <https://doi.org/10.2118/84299-MS>.
- Farid, M. F., Arns, J. Y., Pinczewski, W. V. et al. 2016. Experimental and Numerical Investigation on Stress Dependence of Sandstone Electrical Properties and Deviations from Archie's Law. Paper presented at the SPE Annual Technical Conference and Exhibition, Dubai, UAE, 26–28 September. SPE-181484-MS. <https://doi.org/10.2118/181484-MS>.
- Garboczi, E. J. 1998. Finite Element and Finite Difference Programs for Computing the Linear Electric and Elastic Properties of Digital Images of Random Materials. Internal technical report 6269, National Institute of Standards and Technology, Gaithersburg, Maryland, USA.
- Gomez, C. T., Dvorkin, J., and Vanorio, T. 2010. Laboratory Measurements of Porosity, Permeability, Resistivity, and Velocity on Fontainebleau Sandstones. *Geophysics* **75** (6): E191–E204. <https://doi.org/10.1190/1.3493633>.
- Han, M., Youssef, S., Rosenber, E. et al. 2009. Deviation from Archie's Law in Partially Saturated Porous Media: Wetting Film versus Disconnectedness of the Conducting Phase. *Phys Rev E* **79** (3): 31127. <https://doi.org/10.1103/PhysRevE.79.031127>.
- Hilpert, M. and Miller, C. T. 2001. Pore-Morphology-Based Simulation of Drainage in Totally Wetting Porous Media. *Adv Water Resour* **24** (3–4): 243–255. [https://doi.org/10.1016/S0309-1708\(00\)00056-7](https://doi.org/10.1016/S0309-1708(00)00056-7).
- Jones, A. C., Arns, C. H., Hutmacher, D. W. et al. 2009. The Correlation of Pore Morphology, Interconnectivity and Physical Properties of 3D Ceramic Scaffolds with Bone Ingrowth. *Biomaterials* **30** (7): 1440–1451. <https://doi.org/10.1016/j.biomaterials.2008.10.056>.
- Katsevich, A. 2004. An Improved Exact Filtered Backprojection Algorithm for Spiral Computed Tomography. *Adv Appl Math* **32** (4): 681–697. [https://doi.org/10.1016/S0196-8858\(03\)00099-X](https://doi.org/10.1016/S0196-8858(03)00099-X).
- Knackstedt, M. A., Arns, C. H., Sheppard, A. P. et al. 2007. Pore Scale Analysis of Electrical Resistivity in Complex Core Material. International Symposium of the Society of Core Analysts, Calgary, Alberta, Canada, 10–12 September. SCA2007-33.
- Kumar, M., Senden, T. J., Arns, C. H. et al. 2011. Probing the Archie's Exponent under Variable Saturation Conditions. *Petrophysics* **52** (2): 124–134.

- Lee, J. S. 1983. Digital Image Smoothing and the Sigma Filter. *Comput Vision Graphics Image Process* **24** (2): 255–269. [https://doi.org/10.1016/0734-189X\(83\)90047-6](https://doi.org/10.1016/0734-189X(83)90047-6).
- Montaron, B. 2009. Connectivity Theory—A New Approach to Modelling Non-Archie Rocks. *Petrophysics* **50** (2): 102–115.
- Nixon, M. S. and Aguado, A. S. 2012. *Feature Extraction & Image Processing for Computer Vision*. Waltham, Massachusetts, USA: Academic Press.
- Porter, C. R. and Carothers, J. E. 1970. Formation Factor-Porosity Relation Derived from Well Log Data. *The Log Analyst* **12** (1): 16–26.
- Reddinger, W. 1998. CT Image Quality, http://www.e-radiography.net/mrict/CT_IQ.pdf (accessed 5 March 2019).
- Ronneberger, O., Fischer, P., and Brox, T. 2015. U-Net: Convolutional Networks for Biomedical Image Segmentation. Paper presented at the 18th International Medical Image Computing and Computer-Assisted Intervention, Munich, Germany, 5–9 October. https://doi.org/10.1007/978-3-319-24574-4_28.
- Saadatfar, M., Kabla, A., Senden, T. J., et al. 2005. The Geometry and Number of Contacts of Monodisperse Sphere Packs Using X-Ray Tomography. In *Powders and Grains 2005*, CRC Press London, <https://doi.org/10.1201/NOE0415383486>.
- Sakellariou, A., Arns, C. H., Sheppard, A. P. et al. 2007. Developing a Virtual Materials Laboratory. *Mater Today* **10** (12): 44–51. [https://doi.org/10.1016/S1369-7021\(07\)70307-3](https://doi.org/10.1016/S1369-7021(07)70307-3).
- Sheppard, A. P., Arns, C. H., Sakellariou, A. et al. 2006. Quantitative Properties of Complex Porous Materials Calculated from X-Ray μ CT Images. *Dev X-Ray Tomogr V* **631811**. <https://doi.org/10.1117/12.679205>.
- Sheppard, A. P., Sok, R. M., and Averdunk, H. 2004. Techniques for Image Enhancement and Segmentation of Tomographic Images of Porous Materials. *Physica A* **339** (1–2): 145–151. <https://doi.org/10.1016/j.physa.2004.03.057>.
- Shikhov, I. and Arns, C. H. 2013. A Comparison of Pore-Scale Centrifuge Mercury Intrusion and Porous Plate Capillary Drainage Numerical Experiments. Paper presented at the International Symposium of the Society of Core Analysts, Napa Valley, California, USA, 16–19 September. SCA2013-49.
- Shikhov, I. and Arns, C. H. 2015. Evaluation of Capillary Pressure Methods via Digital Rock Simulations. *Transp Porous Media* **107** (2): 623–640. <https://doi.org/10.1007/s11242-015-0459-z>.
- Sprawls, P. 1995. Image Characteristics and Quality. In *The Physical Principles of Medical Imaging*, second edition. Montreat, North Carolina, USA: Sprawls Educational Foundation. <http://www.sprawls.org/ppmi2/IMGCHAR>.
- Timur, A., Hemphkins, W. B., and Worthington, A. E. 1972. Porosity and Pressure Dependence of Formation Resistivity Factor for Sandstones. Paper presented at the CWLS 4th Formation Evaluation Symposium, Calgary, Alberta, Canada, 9–10 May.
- Varslot, T., Kingston, A., Myers, G. et al. 2011. High-Resolution Helical Cone-Beam Micro-CT with Theoretically Exact Reconstruction from Experimental Data. *Med Phys* **38** (10): 5459–5476. <https://doi.org/10.1118/1.3633900>.
- Wilson, O. B. 2004. *The Influence of Porous Plates on Effective Drainage and Imbibition Rates*. PhD dissertation, Norwegian University of Science and Technology, Trondheim, Norway.
- Winsauer, W. O., Shearin, H. M. Jr, Masson, P. H. et al. 1952. Resistivity of Brine-Saturated Sands in Relation to Pore Geometry. *AAPG Bull* **36** (2): 253–277. <https://doi.org/10.1306/3D9343F4-16B1-11D7-8645000102C1865D>.
- Yanici, S., Arns, J. Y., Cinar, Y. et al. 2013. Percolation Effects of Grain Contacts in Partially Saturated Sandstones: Deviations from Archie's Law. *Transp Porous Media* **96** (3): 457–467. <https://doi.org/10.1007/s11242-012-0099-5>.